Interface Engineered $W_xC@WS_2$ Nanostructure for Enhanced Hydrogen Evolution Catalysis

*Fengmei Wang, Peng He, Yuanchang Li, Tofik Ahmed Shifa, Ya Deng, Kaili Liu, Qisheng Wang, Feng Wang, Yao Wen, Zhenxing Wang, Xueying Zhan, Lianfeng Sun, and Jun He**

For increasing scalability and reducing cost, transition metal dichalcogenides-based electrocatalysts presently have been proposed as substitutes for noble metals to generate hydrogen, but these alternatives usually suffer from inferior performance. Here, a *Ravenala leaf*-like $W_xC@WS_2$ heterostructure is grown via carbonizing WS_2 nanotubes, whose outer walls being partially unzipped along with the W_x C "leaf-valves" attached to the inner tubes during the carbonization process. This heterostructure exhibits a catalytic activity for hydrogen evolution reaction with low overpotential of 146 mV at 10 mA cm^{-2} and Tafel slope of 61 mV per decade, outperforming the performance of WS_2 nanotubes and W_xC counterparts under the same condition. Density functional theory calculations are performed to unravel the underlying mechanism, revealing that the charge distribution between W_xC and WS_2 plays a key role for promoting H atom adsorption and desorption kinetics simultaneously. This work not only provides a potential low-cost alternative for hydrogen generation but should be taken as a guide to optimize the catalyst structure and composition.

1. Introduction

Hydrogen, as a sustainable and clean candidate, has been devoted considerable attention to satisfy the growing global energy demand and curb environmental pollution.[1] To achieve a superb H_2 evolution rate, precious metals, such as Pt, Pd, etc., are regarded as benchmark catalysts for the hydrogen evolution reaction (HER). Nevertheless, their scarcity and high-cost are major obstacles toward wide practical utilization.[2] Until now, extensive exploration of alternatively inexpensive and earth-abundant electrocatalysts with high durability is stimulated.[3–5] Transition metal dichalcogenides (TMDs), such as WS_2,[4,6] have gained widespread attention as HER electrocatalysts. Enormous experimental[7] and theoretical[8,9] results corroborate the indispensability of their edges rather than basal plane $\left(\triangle G_H^{\circ} \geq 2.23\,\text{eV}\right)$ to catalyze the HER process. The low free energy of hydrogen adsorption $\left(\triangle G_H^{\circ} \approx -0.04\,\text{eV}\right)$ on the edge of WS_2 endows a fertile ground to auspiciously catalyze hydrogen evolution.[9] However, numerous follow-up studies have so far demonstrated the limited improvement via phase conversion[6,10] or layer alignment.[11] For further improving the HER activity, researchers explored various WS_2-based hybrids combined with conductive nanocarbon materials,[12–14] including graphene and carbon nanotubes. This kind of heterogeneous structure features the advantages of (1) preventing the nanomaterials from aggregation and increasing the dispersion of the active sites, (2) enhancing the conductivity of the electrocatalysts, and (3) improving the activity via optimizing the hydrogen adsorption free energy due to strong chemical attachment and electrical coupling between them.[15] Thus, the catalytic property of the materials "worked" with WS_2 is also vital.

Abundant reported indications disclose that the introduction of carbon into the lattices of non-noble metals, which could endow them with higher d-band electronic density of states at the Fermi level, confers them the noble metal-like (Pt, Pd) catalytic properties.[16,17] Among them, tungsten carbides, such as WC[18] and W_2C,[19] have been suggested as promising electrocatalysts[16] for HER owing to impressive hydrogenation catalytic performance. Their high corrosion resistance and superior

F. M. Wang, T. A. Shifa, Y. Deng, K. Liu, F. Wang, Y. Wen, Prof. Z. Wang, X. Zhan, Prof. L. Sun, Prof. J. He
CAS Center for Excellence in Nanoscience
CAS Key Laboratory of Nanosystem and Hierarchical Fabrication
National Center for Nanoscience and Technology
Beijing 100190, China
E-mail: hej@nanoctr.cn

F. M. Wang, T. A. Shifa, Y. Deng, K. Liu, F. Wang, Y. Wen
University of Chinese Academy of Sciences
Beijing 100049, P. R. China

P. He
State Key Laboratory of Chemical Resource Engineering
Beijing University of Chemical Technology
Beijing 100029, P. R. China

Prof. Y. Li
National Center for Nanoscience and Technology
Beijing 100190, China

Dr. Q. Wang
Department of Electrical and Computer Engineering
National University of Singapore
117576, Singapore

DOI: 10.1002/adfm.201605802

© 2017 WILEY-VCH Verlag GmbH & Co. KGaA, Weinheim

electronic conductivity[20,21] make them suitable candidates for catalyzing the conversion of H^+ to H_2 in acidic media. Meanwhile, they are usually used as supports to reduce Pt loading without compromising electrolysis efficiency,[20] or composited with carbon nanotubes for increased HER performance.[21] Unfortunately, it has remained a great challenge to controllably synthesize the tungsten carbides without the contamination of a graphitic coke and carbon layer,[22] and improve the electrocatalytic activity for hydrogen generation without the assistance of noble metals due to large hydrogen binding energy, which holds back the hydrogen desorption process.[23] This drawback could be alleviated via rationally designing a hybrid structure and engineering the interface therein. If such a hybrid is made with WS_2, it would have the benefits of extending the noble metal resemblance of W_xC to WS_2 and improving the hydrogen desorption ability of W_xC surface through electron transfer. The latter concomitantly improves hydrogen adsorption ability of WS_2 basal planes. Thus, it appears quite reasonable to engineer this interface in pursuit of enhanced catalytic activity. Herein, we rationally fabricate *Ravenala leaf*-like $W_xC@WS_2$ heterostructure. In this reaction process, the outer walls of the few-walled WS_2 nanotubes (NTs) were partially unzipped along with the emergence of nanoscale W_xC "leaf-valves," which are attached onto the inner tubes. Impressively, this heterostructure demonstrates a recorded catalytic activity to generate hydrogen gas with low onset overpotential of 70.3 mV, overpotential of 146 mV at 10 mA cm^{-2}, Tafel slope of 61 mV per decade, which outperforms the WS_2 NTs and W_xC counterparts under the same measurement condition. It also exhibits a prominent long-time stability with little degradation of the catalytic ability. Further, density functional theory (DFT) calculations were performed to unravel the underlying mechanism, revealing the charge distribution between W_xC and WS_2 plays a key role for promoting H atom adsorption and desorption kinetics simultaneously. The electron transfer from W_xC to WS_2 contributes to improve the bonding of the attached H atom both on the W_xC surface and also on the WS_2 basal plane during the hydrogen evolution process.

2. Results and Discussion

We synthesized $W_xC@WS_2$ heterostructure on carbon fibers (CFs) through carbonizing WS_2 NTs.[24–26] The morphology and composition of $W_xC@WS_2$-XX (XX represents the carbonization time; Figure S1 and Note I, Supporting Information) can be controlled by the reaction time. Transmission electron microscopic (TEM) image of $W_xC@WS_2$-10 (**Figure 1**a) shows partially unzipped nanotube with an interplanar distance of 0.618 nm being ascribed to (002) planes of WS_2 in the corresponding high-resolution TEM image (HRTEM, Figure 1b). A closer look at the nanobelt attached to the nanotube (Figure 1b,c) reveals the incorporated WS_2 (101) and W_3C (211) with the lattice distance of 0.267 and 0.206 nm, respectively. Energy-dispersive X-ray spectroscopy (EDX) mapping (Figure 1d and Figure S2, Supporting Information) displays that the S element is mainly situated in the middle, while the C element located in the exterior of the nanobelt. Notably, the *Ravenala leaf*-like nanoribbons were produced when the reaction time is increased to 20 min (Figure 1e and Figure S2, Supporting Information), and new domain with an interplanar spacing of 0.227 nm corresponds to the (101) plane of

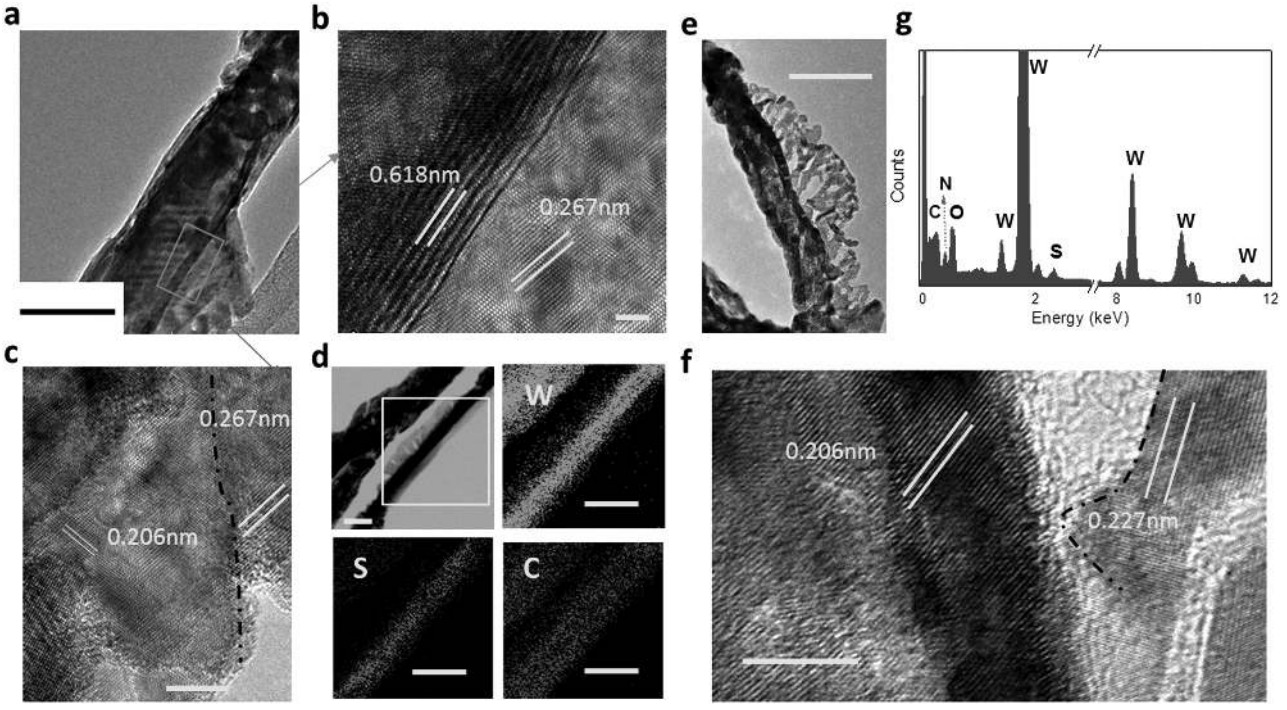

Figure 1. a–d) TEM (a), HRTEM (b,c) images, and EDX mapping (d) of $W_xC@WS_2$-10. Scale bar: 50 nm (a), 2 nm (b), 5 nm (c), and 100 nm (d). e–g) TEM (e), HRTEM (f) images, and EDX spectrum (g), N peak emanated from the SiN-coated TEM grid) of $W_xC@WS_2$-20, demonstrating the existence of WS_2 and W_xC. Scale bar: 50 nm (e) and 5 nm (f).

© 2017 WILEY-VCH Verlag GmbH & Co. KGaA, Weinheim

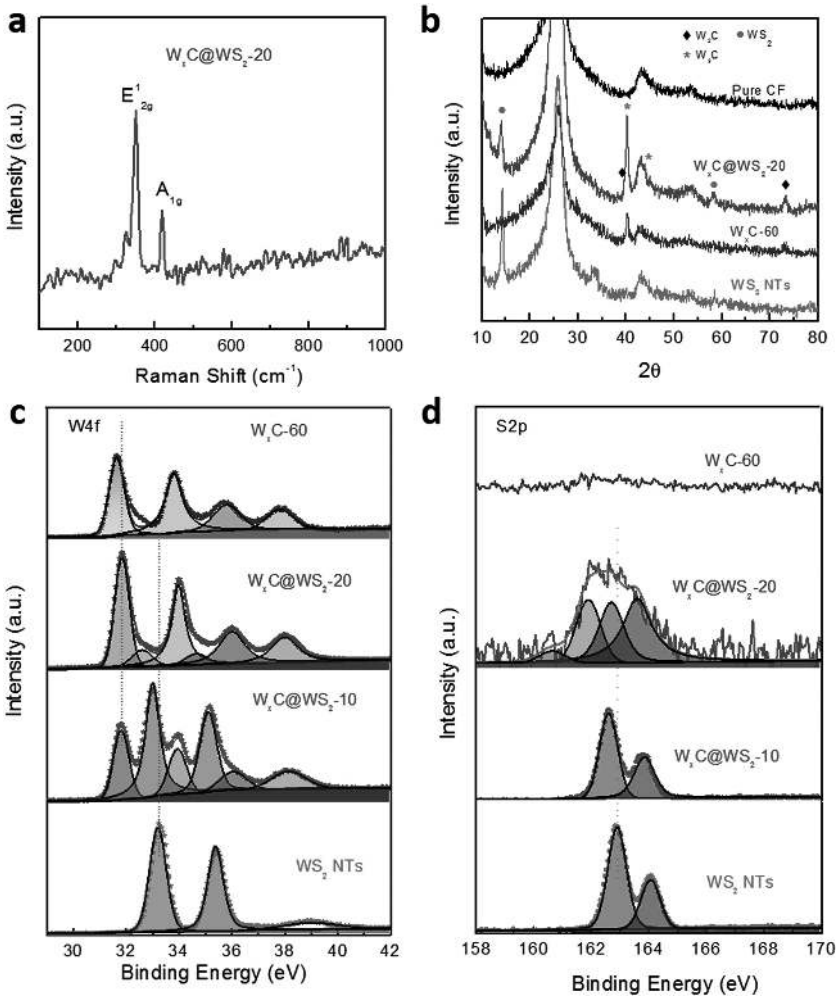

Figure 2. a) Raman spectrum of $W_xC@WS_2$-20. b) Representative XRD diffractograms of pure CF, $W_xC@WS_2$-20, W_xC-60, and WS_2NTs on CFs. c,d) XPS high-revolution scans of W 4f (c) and S 2p (d) of $W_xC@WS_2$ with reaction time of 10, 20, and 60 min, compared with those of WS_2 NTs.

hexagonal W_2C (Figure 1f, confirmed by X-ray diffraction (XRD) below).[27] The substantial amount of W accompanied by C and S elements are distributed in $W_xC@WS_2$-20 (Figure 1g). Meanwhile, the band shifts around 350 and 417 cm^{-1} in the Raman spectra (**Figure 2**a and Figure S3a, Supporting Information) are attributed to the E^1_{2g} and A_{1g} phonon modes of WS_2. These results are consistent with the observation of XRD patterns (Figure 2b and Figure S3b, Supporting Information), which also reveals the existence of WS_2 (PDF#08-0237), W_3C (PDF#42-0853), and W_2C (PDF#02-1134) phase in $W_xC@WS_2$-20. Given this, hydrogen first reacts with sulfur atoms in the defect of WS_2[25] to unzip the NT shell, followed by CH_4 attack to form tungsten carbides.[26,28] Finally, the WS_2 NTs were completely transformed into textured tungsten carbide nanoribbons when the reaction time reaches 60 min (W_xC-60, Figure S1g–k, Supporting Information).

X-ray photoelectron spectroscopy (XPS) analysis (Figure 2c,d and Figure S4a, Supporting Information) was conducted to probe the elemental composition of $W_xC@WS_2$ samples. In $W_xC@WS_2$-10 and $W_xC@WS_2$-20, high-resolution W4f spectra (Figure 2c) demonstrate that the peaks ($W4f_{7/2}$) at 31.8 and 33.0 eV are attributed to W−C[25] and W−S bonding, respectively. From the deconvolution of the XPS spectra, the W_xC content is estimated to be ≈37.5% and ≈78% in $W_xC@WS_2$-10 and $W_xC@WS_2$-20. A doublet at 35.92/38.05 eV likely originates from the surface oxidation. In parallel, the peaks at around 162.59 ($S2p_{3/2}$) and 163.75 eV ($S2p_{1/2}$) in the deconvolution of S2p (Figure 2d) are stemmed from WS_2, but they are slightly shifted to lower binding energies compared to those of WS_2 NTs (162.89 and 164.05 eV),[25] suggesting the introduction of sulfur deficiency or interaction between sulfide and carbides. Particularly, the new peaks at the lower binding energies (≈160.9 and 162.1 eV) are supposed to be due to the electronic redistribution around the sulfur atom via charge transfer, strongly suggesting the establishment of coupling interface between W_xC and WS_2. As will be demonstrated below, such a charge transfer is critical for the superior catalytic activity of $W_xC@WS_2$.

To characterize the electrocatalytic activities of various materials toward HER, the samples were directly used as working electrode without any pretreatment. Linear sweep voltammetry curves with iR correction (**Figure 3**a) exhibits that use of $W_xC@WS_2$-20 electrode generates a current density of −10 mA cm^{-2} at −146 mV (vs reversible hydrogen electrode (RHE), η_{10}), roughly 172.7 and 46 mV lower than the potentials required for WS_2 (−318.7 mV) and W_xC-60 (192 mV) for obtaining the same current density, respectively. The corresponding Tafel slope (Figure 3b) of 61 mV per decade for $W_xC@WS_2$-20 is also much smaller than that of WS_2 (≈110 mV per decade) and W_xC-60 (≈68 mV per decade), suggesting a two-electron transfer process following Volmer–Heyrovsky mechanism. This performance compares or even surpasses those of all previously reported other electrocatalysts (Table S2, Supporting Information) for HER in acidic media, such as 1T-WS_2 nanosheets (−142 mV at 10 mA cm^{-2}; 70 mV per decade),[10] rGO/WS_2 nanosheets (−229 mV at 10 mA cm^{-2}; 73 mV per decade),[13] WC-CNTs (−145 mV at 10 mA cm^{-2}; 72 mV per decade),[21] WP_2 submicroparticle (−161 mV at 10 mA cm^{-2}, 57 mV per decade),[29] WP NAs (−130 mV at 10 mA cm^{-2}, 69 mV per decade),[30] and Mo_2C/GCSs (−200 mV at 10 mA cm^{-2}, 62.6 mV per decade).[31] More importantly, the exchange current density (j_0) of 4.2×10^{-5} A cm^{-2} for $W_xC@WS_2$-20 exceeds three times that of W_xC-60 (1.4×10^{-5} A cm^{-2}), accounting for its outstanding catalytic ability (Table S1, Supporting Information). At the same time, other $W_xC@WS_2$ electrodes were also investigated (Figure 3c and Figure S5, Supporting Information). Among them, $W_xC@WS_2$-20 exhibits the best HER activity in acidic media. In a sharp contrast to WS_2 and W_xC,

© 2017 WILEY-VCH Verlag GmbH & Co. KGaA, Weinheim

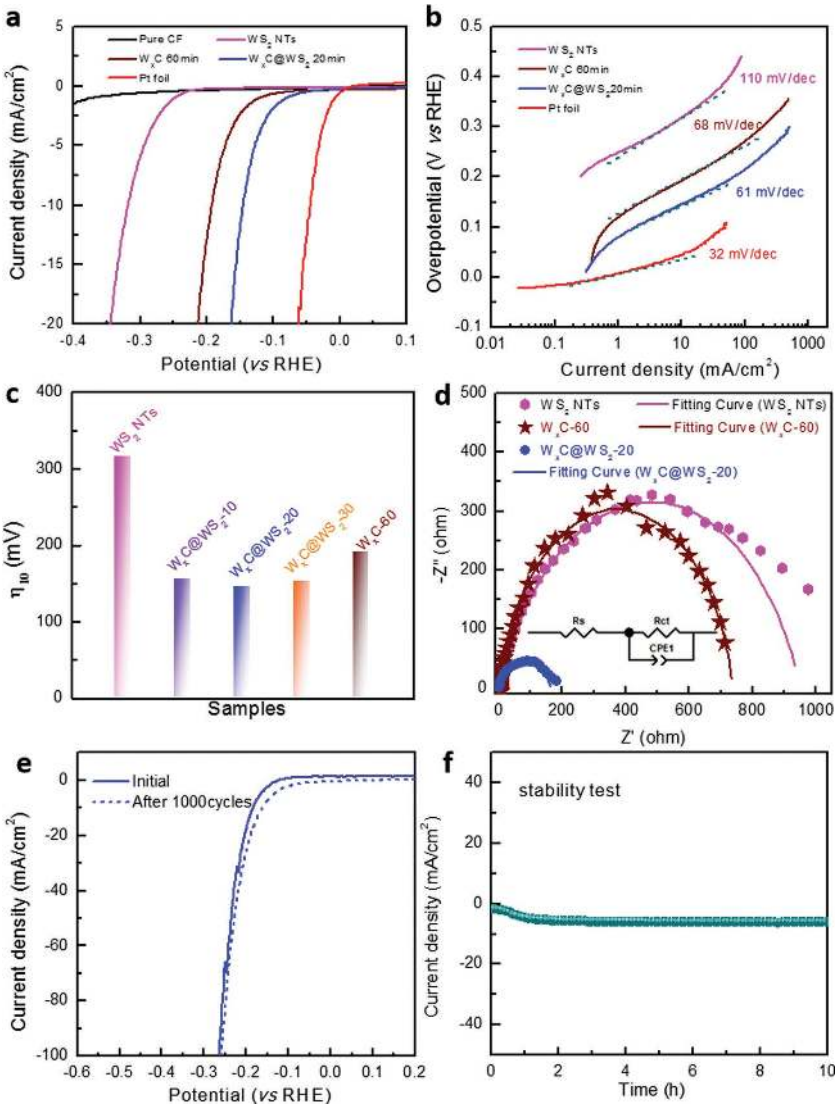

Figure 3. a,b) Polarization curves and corresponding Tafel plots for HER of various electrodes. Scan rate: 5 mV s^{-1}. c) Comparison of the overpotential of different $W_xC@WS_2$ electrocatalysts with W_xC and WS_2 ones. d) Electrochemical impedance spectroscopy (EIS) Nyquist plots at −0.15 V (vs RHE) for $W_xC@WS_2$-20, W_xC-60, and WS_2 NTs electrode. The data were fitted using the modified Randles circuits (the inset). e) The comparison of polarization curves of $W_xC@WS_2$-20 after continuous sweeps at 100 mV s^{-1} in 0.5 M H_2SO_4. f) The chronoamperometry measurement of $W_xC@WS_2$-20 under a fixed overpotential of 150 mV (vs RHE).

the much lower onset potential (80 mV) of $W_xC@WS_2$ than W_xC (117 mV) and WS_2 (210 mV) further confirms the remarkably enhanced catalytic activity in acidic media (Figure S6 and Table S1, Supporting Information).

The double-layer capacitances (C_{dl}; Figure S7a–c, Supporting Information) extracted from cyclic voltammetry (CV) measurements reveal the increased electrochemical surface areas for $W_xC@WS_2$-20 (2.13 mF cm^{-2}) and W_xC-60 (3.18 mF cm^{-2}) compared to that of WS_2 NTs.[25] The W_xC-60 electrode possesses a little larger electrochemical surface area, but it demonstrated inferior HER performance as compared to $W_xC@WS_2$-20. Given this, electrochemical impedance spectroscopy (EIS; Figure 3d and Figure S5c, Supporting Information) was collected to gain further insight into the electrocatalytic activity of $W_xC@WS_2$-20 and W_xC-60 during the HER process. The smaller semicircular arc (162.3 Ω) for $W_xC@WS_2$-20 than that for W_xC-60 (745.1 Ω) and WS_2 NTs (942.4 Ω) proves the markedly faster H_2 evolution kinetics. This suggests the interaction between W_xC and WS_2 is strongly speculated to boost the HER activity of $W_xC@WS_2$-20.

To this end, the long-term stability of $W_xC@WS_2$-20 was characterized through continuous 1000 cyclic voltammetry cycles. A negligible decay (Figure 3e) is observed at high current density. During 10 h electrocatalysis tests at a constant potential of −0.15 V (vs RHE Figure 3f), $W_xC@WS_2$-20 also shows negligible decay in current density. This suggests good stability of $W_xC@WS_2$-20, which is also confirmed by XPS analysis in Figure S4 (Supporting Information), demonstrating no obvious change in the chemical state and composition. The peak for $S2p_{3/2}$ at the low binding energy (≈160.9 eV) emerges clearly, further indicating the disappearance of tungsten oxide after the stability test. Additionally, scanning electron microscopic (SEM) image, EDX spectrum, and XRD (Figure S8, Supporting Information) characterization also suggest the excellent stability of $W_xC@WS_2$ electrocatalyst in acidic media.

Three points can be gleaned from the aforementioned results. First, W_xC is transformed from the unzipped WS_2 nanotubes with $x \geq 2$. Second, it is the synergistic effect of W_xC and WS_2 that gives a tunable HER ability. Third, the active site predominantly lies on the terrace rather than the edge. With these facts in hand, we performed a series of DFT calculations[32,33] to gain some insight into the improved catalytic activity of $W_xC@WS_2$ complex (Note II, Supporting information). In this regard, the hexagonal W_2C, plotted in **Figure 4**a, is taken as an example to illustrate the HER ability. Similar to WS_2, it also consists of the triple-layer configuration, but by contrast, it is composed of a layer of C sandwiched between two layers of W.[34] We investigated the Gibbs free energy ($\triangle G_{H*}$)[8,32] required for hydrogen adsorption on the (0001) surface with different hydrogen coverage (θ_H) (Figure 4b), and the results are summarized in Table S3 (Supporting Information). A $\triangle G_{H*}$ value close to zero indicates the superior HER activity with the optimal balance between the absorption and the removal of hydrogen atom on the active sites.[33] It is found that the $\triangle G_{H*}$ monotonously increases from −0.37 to −0.24 eV in Figure 4c as the θ_H increases from 0.11 to 1. Such a $\triangle G_{H*}$ usually corresponds to a moderate HER ability, well-consistent with our experimental results shown in Figure 3a. Nevertheless, our synthesized samples are in

© 2017 WILEY-VCH Verlag GmbH & Co. KGaA, Weinheim

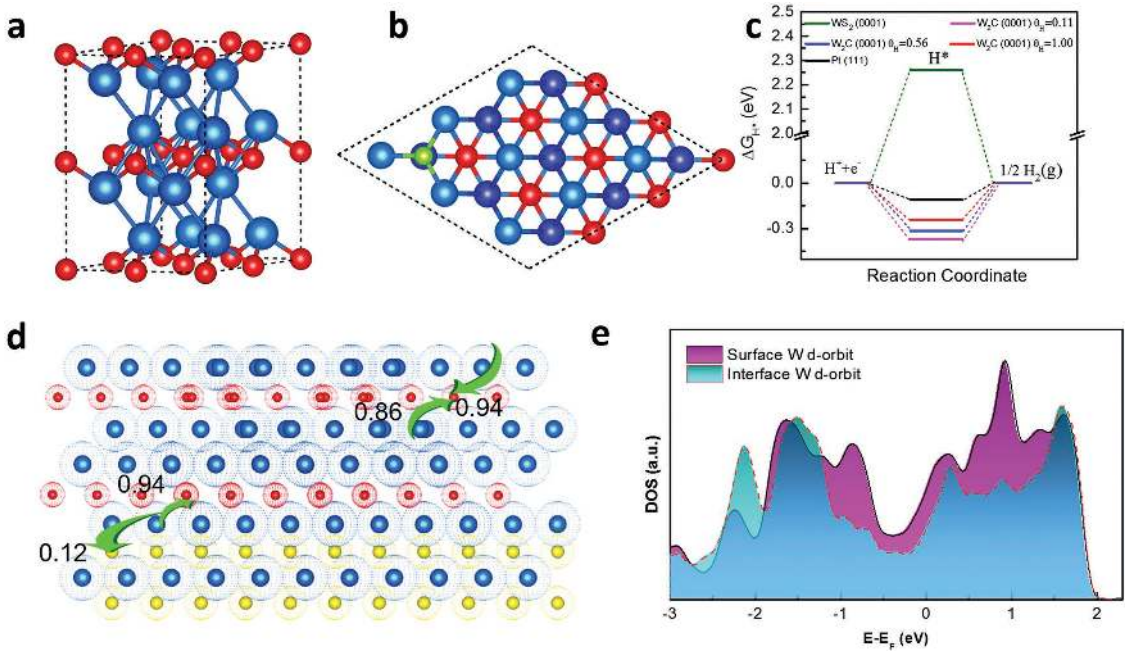

Figure 4. a) Crystal structure of the hexagonal W_2C with the CdI_2 type. Red and cyan balls are the C and W atoms, respectively. b) A hydrogen atom adsorbed on W_2C (0001) surface with the coverage of 1/9. Blue and cyan balls are the W atom at the top and bottom surfaces. Green ball is the adsorbed hydrogen atom. c) Free energy diagram of HER under different H* coverage (θ_H = 0.11, 0.56, and 1), as well as the comparison with Pt(111) and WS_2 terrace sites. d) Charge redistribution in $W_2C@WS_2$ heterostructure. The arrows denote the electron transfer direction. The unit, |e|. Blue, red, and yellow balls are the W, C, and S atoms. e) The density of states (DOS) comparison of the W on the surface and interface around the Fermi level.

fact W_xC ($x \geq 2$), and the modeled W_2C gives only the upper bound for the hydrogen binding energy (Note II, Supporting Information). In other words, the actual $\triangle G_{H*}$ on W_xC must be smaller than –0.24 eV. This implies that the W_xC binds H atoms too tightly to desorb, hence hindering the H_2 evolution on its surface.

On the other hand, H atoms are hardly adsorbed on the terrace of WS_2 due to the large $\triangle G_{H*}$ of 2.26 eV (Figure 4c). When interfacing W_2C with WS_2, it is interestingly found that there occurs an apparent electron transfer of 0.12 |e| from the outmost W of W_2C to WS_2, in addition to the bonding with C atoms, illustrated in Figure 4d and Figure S9a,b (Supporting Information). The additional loss of electron from this kind of W strongly suggests the decrease of its ability to bind to H atoms (Figure S9c,d, Supporting Information). Note that now the S atoms gains more 0.16|e| than those in pristine WS_2, which should be responsible for the shift of S2p states to the lower binding energy in the XPS analysis. The interfacial charge redistribution is also manifested by the electronic structure analysis (Figure 4e). In comparison with that at the surface of W_2C, the W interfacing to WS_2 shows a significantly reduced density of states around the Fermi level, which definitely means a weaker bonding to the attached H atom and the $\triangle G_{H*}$ more close to zero for the interfacial W. It is worth to emphasize that the electron transfer and the ultimate catalytic ability of interfacial W must be *x*-dependent, so the samples with the different carbonization time give rise to the remarkably distinct HER performances. When the carbonization time is appropriately controlled, the $\triangle G_{H*}$ can become exactly zero, thus leading to the best catalytic ability. Apart from the $W_2C@WS_2$ interface, the mixed (W—C—S) complex may also arise from the carbonization process. However, our calculations reveal that this is not the case for the observed superior HER ability due to the impermeability between W_2C and WS_2 (Note II, Supporting information).

3. Conclusion

In all, the fabricated $W_xC@WS_2$ hybrid electrocatalyst exhibits improved HER performance than that of W_xC and WS_2, with respect to pertinent HER, including the overpotential, Tafel slope, and exchange current density. The strong interface interaction and redistribution of electrons between W_xC and WS_2 facilitate the dynamical process to generate hydrogen molecules. Apart from this merit, the electrocatalyst is prepared through direct growth on the conductive substrate without complicated pre- or postprocessing, which is convenient and reliable for practical application. The carbonization time is the only factor to be optimized in further research. What is more, our work should be taken as a guide to design effective noble metal-free catalysts and a new path for improving the catalyst structure and composition. Introducing a novel material with the property of easily adsorbed H into another material, from which H atoms desorb easily, provides further avenues to construct an efficient HER catalyst. It synergistically promotes proton adsorption and reduction kinetics by charge distribution. These findings provide clear evidence that the well-designed noble-metal free hybrid counterparts have great potential for highly efficient electrocatalysis of HER to substitute noble metals.

© 2017 WILEY-VCH Verlag GmbH & Co. KGaA, Weinheim

4. Experimental Section

Synthesis of $W_xC@WS_2$ Nanomaterials: The uniform WS_2 NTs on CFs were presynthesized by sulfurization reaction of WO_3 nanowires in two-zone furnace.[24,25] The previously described procedure was utilized (Supporting Information). To prepare the $W_xC@WS_2$ samples, the WS_2 NTs on CFs were heated up to 750 °C with a flowing mixture of Ar and H_2 (20:7, 270 sccm) at a heating rate of 10 °C min^{-1}, then the CH_4 (5 sccm) gas was inlet into the tube and further heated at 750 °C for different reaction time (5, 10, 20, 30, and 60 min) to obtain $W_xC@WS_2$ heterostructures. After the reaction process, the methane was turned off and the furnace cooled down under a flow of argon and hydrogen, where materials were then removed. The mass loading of the electrocatalyst is about 0.30 ± 0.03 mg cm^{-2}, determined through using an electronic balance (BT 125D) with 10 µg accuracy.

Characterization: The morphologies were observed under Hitachi S4800 SEM and FEI TecnaiF20 TEM operated at 200 kV. Scanning transmission electron microscopic (STEM)-EDX elemental mapping and EDX line scan were recorded on a JEM-2100F apparatus at an accelerating voltage of 200 kV. The EDX spectrum was collected on the SiN-coated TEM grid to confirm the incorporated C element in the heterostructures. Thus, the N peak in the EDX spectrum emanated from the SiN-coated TEM grid. XPS was recorded on ESCALAB 250 Xi system of Thermo Scientific, where the analysis chamber was 1.5×10^{-9} Mbar and the X-ray spot was 500 µm. The samples after activation process and the stability measurement were dried in the tube furnace with flowing of ultrapure N_2 at 60 °C. And then they were protected in the serum bottle filled with Ar gas from being oxidized in the air for further XPS analysis. Raman scattering was performed on a confocal microscope-based Raman spectrometer (Renishaw In Via) in ambient air environment with an excitation laser line of 532 nm. The XRD patterns were recorded on the D/MAX-TTRIII (CBO) diffractometer equipped with Cu Kα radiation (λ = 1.5418 Å). The pH of the electrolyte was tested on the METTLER TOLEDO pH meter (FE20).

Electrochemical Measurements: All electrochemical experiments were conducted on CHI 660D potentiostat in a three-electrode electrochemical compression cell containing 0.5 M H_2SO_4 (pH = 0.67). Each measurement was performed in the solution continuously purged with N_2 (99.999%) to eliminate dissolved oxygen. A piece of CF covered by nanomaterials with a test area of about 0.6 cm^2 acted as working electrode, and a saturated calomel electrode and Pt wire or Glass Carbon electrode served as reference electrode and counter electrode, respectively. The electrocatalytic activities of these samples were examined by polarization curves using linear sweep voltammetry at a scan rate of 5 mV s^{-1}. The commercial Pt foil (99.99%) was also used as a reference sample. All potentials were calibrated to a RHE, and the polarization curves demonstrated were corrected for *iR* losses. EIS was carried out from 2 MHz to 10 mHz with an amplitude of 10 mV at a constant 0.15 V. The corresponding circuit model fitting analysis showed the same equivalent circuit consisting of a series resistance (R_s), constant phase element, and electrochemical charge transfer resistance (R_{ct}). The electrochemical stability of the catalyst was conducted by cycling the potential between –0.1 to 0.28 V at a scan rate of 100 mV s^{-1}. The chronoamperometry was measured at a potential of –0.15 V after equilibrium with the glass carbon as the counter electrode. To estimate the electrochemical active surface areas of the catalysts, CV curves were tested via measuring C_{dl} under the potential window of 0.1–0.2 V with various scan rate (40, 80, 120, 160, 200 mV s^{-1}).

Theoretical Calculations: All calculations were performed within the framework of DFT using the Vienna Ab initio Simulation Package.[35] The electron–ion interaction and the exchange-correlation effect were described by the projector-augmented wave[36] method and the Perdew–Burke–Ernzerhof functional[37] based on generalized gradient approximation. The cutoff energy was set to 680 eV. During the calculations of H adsorption, the W_2C (0001) was modeled by two W_2C triple layers in the vertical direction and a 3 × 3 supercell in the horizontal direction. For $W_2C@WS_2$, an additional WS_2 triple layer is capped on the W_2C (0001). In all the calculations, the bottom W_2C triple layer is fixed at its bulk configuration while the other atoms were fully relaxed until the residual forces were less than 0.02 eV $Å^{-1}$.

Supporting Information

Supporting Information is available from the Wiley Online Library or from the author.

Acknowledgements

F.M.W. and P.H. contributed equally to this work. This work was supported by the National Natural Science Foundation of China (Nos. 21373065, 61474033, 61574050, and 11674071), Strategic Priority Research Program of the Chinese Academy of Sciences (Grant No. XDA09040201), 973 Program of the Ministry of Science and Technology of China (No. 2012CB934103), and CAS Key Laboratory of Nanosystem and Hierarchical Fabrication. The authors also gratefully acknowledge the support of Youth Innovation Promotion Association CAS.

Received: November 6, 2016
Revised: November 21, 2016
Published online:

[1] a) J. A. Turner, *Science* **2004**, *305*, 5686; b) M. Chhowalla, H. S. Shin, G. Eda, L. J. Li, K. P. Loh, H. Zhang, *Nat. Chem.* **2013**, *5*, 263.
[2] W. Sheng, Z. Zhuang, M. Gao, J. Zheng, J. G. Chen, Y. Yan, *Nat. Commun.* **2015**, *6*, 5848.
[3] a) F. Wang, Y. Li, T. A. Shifa, K. Liu, F. Wang, Z. Wang, P. Xu, Q. Wang, J. He, *Angew. Chem. Int. Ed.* **2016**, *55*, 6919; b) J. Wang, W. Cui, Q. Liu, Z. Xing, A. M. Asiri, X. Sun, *Adv. Mater.* **2016**, *28*, 215; c) M. S. Faber, S. Jin, *Energy Environ. Sci.* **2014**, *7*, 3519; d) J. Tian, Q. Liu, A. M. Asiri, X. Sun, *J. Am. Chem. Soc.* **2014**, *136*, 7587; e) W. Zhu, C. Tang, D. Liu, J. Wang, A. M. Asiri, X. Sun, *J. Mater. Chem. A* **2016**, *4*, 7169.
[4] F. Wang, T. A. Shifa, X. Zhan, Y. Huang, K. Liu, Z. Cheng, C. Jiang, J. He, *Nanoscale* **2015**, *7*, 19764.
[5] a) Y. Jiao, Y. Zheng, K. Davey, S.-Z. Qiao, *Nat. Energy* **2016**, *1*, 16130; b) J. Duan, S. Chen, M. Jaroniec, S. Z. Qiao, *ACS Catal.* **2015**, *5*, 5207; c) Y. Zheng, Y. Jiao, M. Jaroniec, S. Z. Qiao, *Angew. Chem. Int. Ed.* **2015**, *54*, 52; d) B. Bayatsarmadi, Y. Zheng, Y. Tang, M. Jaroniec, S. Z. Qiao, *Small* **2016**, *12*, 3703.
[6] D. Voiry, H. Yamaguchi, J. Li, R. Silva, D. C. B. Alves, T. Fujita, M. Chen, T. Asefa, V. B. Shenoy, G. Eda, M. Chhowalla, *Nat. Mater.* **2013**, *12*, 850.
[7] T. F. Jaramillo, K. P. Jørgensen, J. Bonde, J. H. Nielsen, S. Horch, I. Chorkendorff, *Science* **2007**, *317*, 100.
[8] B. Hinnemann, P. G. Moses, J. Bonde, K. P. Jørgensen, J. H. Nielsen, S. Horch, I. Chorkendorff, J. K. Nørskov, *J. Am. Chem. Soc* **2005**, *127*, 5308.
[9] C. Tsai, K. Chan, F. Abild-Pedersen, J. K. Norskov, *Phys. Chem. Chem. Phys.* **2014**, *16*, 13156.
[10] M. A. Lukowski, A. S. Daniel, C. R. English, F. Meng, A. Forticaux, R. J. Hamers, S. Jin, *Energy Environ. Sci.* **2014**, *7*, 2608.
[11] Y. Yan, B. Xia, N. Li, Z. Xu, A. Fisher, X. Wang, *J. Mater. Chem. A* **2015**, *3*, 131.
[12] J. Duan, S. Chen, B. A. Chambers, G. G. Andersson, S. Z. Qiao, *Adv. Mater.* **2015**, *27*, 4234.
[13] T. A. Shifa, F. Wang, Z. Cheng, X. Zhan, Z. Wang, K. Liu, M. Safdar, L. Sun, J. He, *Nanoscale* **2015**, *7*, 14760.
[14] J. F. Lin, O. Pitkanen, J. Maklin, R. Puskas, A. Kukovecz, A. Dombovari, G. Toth, K. Kordas, *J. Mater. Chem. A* **2015**, *3*, 14609.

© 2017 WILEY-VCH Verlag GmbH & Co. KGaA, Weinheim

[15] a) Y. Liang, Y. Li, H. Wang, H. Dai, *J. Am. Chem. Soc* **2013**, *135*, 2013; b) S. Chen, J. Duan, Y. Tang, B. Jin, S. Zhang Qiao, *Nano Energy* **2015**, *11*, 11.
[16] W. F. Chen, J. T. Muckerman, E. Fujita, *Chem. Commun.* **2013**, *49*, 8896.
[17] L. H. Bennett, J. R. Cuthill, A. J. McAlister, N. E. Erickson, R. E. Watson, *Science* **1974**, *184*, 563.
[18] a) R. B. Levy, M. Boudart, *Science* **1973**, *181*, 547; b) J. E. Houston, G. E. Laramore, R. L. Park, *Science* **1974**, *185*, 258.
[19] R. D. Armstrong, M. F. Bell, *Electrochim. Acta* **1978**, *23*, 1111.
[20] D. V. Esposito, S. T. Hunt, A. L. Stottlemyer, K. D. Dobson, B. E. McCandless, R. W. Birkmire, J. G. Chen, *Angew. Chem. Int. Ed.* **2010**, *49*, 9859.
[21] X. Fan, H. Zhou, X. Guo, *ACS Nano* **2015**, *9*, 5125.
[22] a) S. T. Hunt, M. Milina, A. C. Alba-Rubio, C. H. Hendon, J. A. Dumesic, Y. Román-Leshkov, *Science* **2016**, *352*, 974; b) P. Xiao, X. Ge, H. Wang, Z. Liu, A. Fisher, X. Wang, *Adv. Funct. Mater.* **2015**, *25*, 1520.
[23] a) D. V. Esposito, S. T. Hunt, Y. C. Kimmel, J. G. Chen, *J. Am. Chem. Soc* **2012**, *134*, 3025; b) D. J. Ham, R. Ganesan, J. S. Lee, *Int. J. Hydrogen Energy* **2008**, *33*, 6865.
[24] F. Wang, J. Li, F. Wang, T. A. Shifa, Z. Cheng, Z. Wang, K. Xu, X. Zhan, Q. Wang, Y. Huang, C. Jiang, J. He, *Adv. Funct. Mater.* **2015**, *25*, 6077.
[25] K. Xu, F. Wang, Z. Wang, X. Zhan, Q. Wang, Z. Cheng, M. Safdar, J. He, *ACS Nano* **2014**, *8*, 8468.
[26] X. Li, J. Zhang, R. Wang, H. Huang, C. Xie, Z. Li, J. Li, C. Niu, *Nano Lett.* **2015**, *15*, 5268.
[27] M. Lewandowski, A. Szymańska-Kolasa, C. Sayag, P. Beaunier, G. Djéga-Mariadassou, *Appl. Catal., B* **2014**, *144*, 750.
[28] B. H. Kim, M. Park, M. Lee, S. J. Baek, H. Y. Jeong, M. Choi, S. J. Chang, W. G. Hong, T. K. Kim, H. R. Moon, Y. W. Park, N. Park, Y. Jun, *RSC Adv.* **2013**, *3*, 18424.
[29] Z. Xing, Q. Liu, A. M. Asiri, X. Sun, *ACS Catal.* **2015**, *5*, 145.
[30] Z. Pu, Q. Liu, A. M. Asiri, X. Sun, *ACS Appl. Mater. Interfaces* **2014**, *6*, 21874.
[31] W. Cui, N. Cheng, Q. Liu, C. Ge, A. M. Asiri, X. Sun, *ACS Catal.* **2014**, *4*, 2658.
[32] J. Kibsgaard, C. Tsai, K. Chan, J. D. Benck, J. K. Norskov, F. Abild-Pedersen, T. F. Jaramillo, *Energy Environ. Sci.* **2015**, *8*, 3022.
[33] C. Tang, L. Gan, R. Zhang, W. Lu, X. Jiang, A. M. Asiri, X. Sun, J. Wang, L. Chen, *Nano Lett.* **2016**, *16*, 6617.
[34] A. S. Kurlov, A. I. Gusev, *Inorg. Mater.* **2006**, *42*, 121.
[35] G. Kresse, J. Furthmüller, *Phys. Rev. B* **1996**, *54*, 11169.
[36] P. E. Blöchl, *Phys. Rev. B* **1994**, *50*, 17953.
[37] J. P. Perdew, K. Burke, M. Ernzerhof, *Phys. Rev. Lett.* **1996**, *77*, 3865.

© 2017 WILEY-VCH Verlag GmbH & Co. KGaA, Weinheim